Investigation on Energy Conversion Instability of Pump Mode in Hydro-Pneumatic Energy Storage System

Chaoyue Wang[1], Fujun Wang[1,2*], Chenfeng Li[3], Wenhao Chen[1], Hao Wang[1], Li Lu[2,4]

[1]*College of Water Resources and Civil Engineering, China Agricultural University, Beijing 100083, China*

[2]*Beijing Engineering Research Center of Safety and Energy Saving Technology for Water Supply Network System, Beijing, 100083, China*

[3]*College of Engineering, Swansea University, Swansea, SA1 8EN, United Kingdom*

[4]*China Institute of Water Resources and Hydropower Research, Beijing, 100038, China*

Abstract: The pump mode of hydro-pneumatic energy storage (HPES) system often experiences off-design conditions due to the boundary pressure rises, and the resultant energy conversion instability has an adverse effect on the system operation. However, the evolution process of this instability and the corresponding flow events are still not fully understood. Experimental and numerical simulation studies of a centrifugal pump with vaned diffuser were conducted in a wide operating range, and the following notable results were obtained. The energy conversion of pump mode shows three typical stages as the pump head increases, stable work→stumbled work→shaky work, corresponding to the inner flow pattern development of stall-free→stall inception→stall deepening. In this evolution process, the attenuation of rotor blade loading gradually spreads from the inlet shroud side to the entire blade. This strengthens the natural adverse potential rothalpy gradient and induces the energetic vortical structures including leading backflow vortices, dynamic stall cells and trailing helical vortices. A strong coupling between large-scale vortical motions and energy conversion is observed and this yields a Logistic growth of the shaft power and pump head fluctuations. The critical condition for the energy conversion instability is the diagnostic function SI=1, and this is recommended for determining the stability limit of the pump mode.

Key Words: Hydro-pneumatic energy storage, pump mode, energy conversion, flow instability, stall

*Corresponding Author.
E-mail Address: wangfj@cau.edu.cn (Fujun Wang), Tel: +86-010-62736972.

1 Introduction

Fossil fuels are still the main source of electricity generation according to the 2021 Big Data Report of Energy. However, fossil fuels are a finite resource and their combustion is an important factor in the global climate crisis [1], and the development and utilization of the renewable energy should be constantly paid attention to. Renewable energy (e.g. solar energy, wind energy, hydro energy, ocean energy, etc.) is characterized by cleanliness and sustainability, and its study is a boost to achieving the "Double Carbon Target" (carbon peak→carbon neutrality) [2]. There are two challenges for integrating the renewable energy into power grids. One is the intermittent caused by seasonal or weather changes, and the other is the heavy dependence of the energy conversion on the spatial distribution [3-4], which causes a mismatch between when/where energy is produced and when/where it is used. Accordingly, energy storage is necessary to guarantee the power quality and improve the system efficiency [5], which has become a hot topic in energy engineering.

Energy storage systems are designed to convert energy from electricity to another form that can be reserved in a suitable medium and then converted back to electricity if it is required [6]. According to the converted energy form, the energy storage technology can be divided into the following types [6-8]: (1) *mechanical energy storage*, such as pumped hydro energy storage (PHES), compressed air energy storage (CAES) and flywheel energy storage; (2) *electro-chemical energy storage*, such as secondary battery, flow battery and metal-air battery; (3) *electro-magnetic energy storage*, such as supercapacitors and superconducting magnetic energy storage; (4) *Hydrogen and thermal energy storage*. In terms of storage capacity and system life, mechanical energy storage is still the dominant technology for large-scale energy storage. Currently, PHES is the most important commercial energy storage technology and makes up 89.3% of the storage capacity in China [9]. The fundamental principle of PHES is to convert energy from electricity to hydraulic potential energy. In the PHES system, the pump mode is driven by the low cost electricity to lift water from the lower reservoir to the upper reservoir, while the turbine mode is driven by the stored water to produce electricity during the peak demand period. PHES is a flexible form of energy storage, which contributes such benefits to power grids as peak shaving and valley-filling, phase modification and frequency control, but the main limitation of it is in determining a suitable site with the economic, environmental and technical availability [5,10-11]. CAES is the other commercially mature energy storage technology, whose fundamental principle is to convert energy from electricity to pressure potential energy. In the CAES system, the compressor mode is driven by the low cost electricity to pressurize air into special vessels, while the turbine mode is driven by the compressed air to produce electricity during the peak demand period. Due to the compressibility of air, CAES includes multiple configurations, such as diabatic CAES, adiabatic CAES, isothermal CAES and isobaric CAES. The diabatic CAES is also known as the traditional isochoric storage technology and is usually based on the geological underground caverns [12-13]. In the compression process (charging), the heat is transferred to the surroundings and is dissipated as waste. In the expansion process (discharging), fossil fuels are used as the external heat source, which can cause the additional pollution. As an improvement, the adiabatic CAES is proposed and developed. The compression heat is transferred and captured in a thermal storage medium, and it is later utilized in the expansion process [14]. The isothermal CAES is designed to maintain a quasi-balanced work process to avoid excessive changes in the compressed air temperature, and the isobaric CAES is proposed to reduce energy consumption in pneumatic systems [15]. For the above two typical mechanical energy storage technologies, the working medium of PHES (water) has a much higher power density, while the working medium of

CAES (air) has a higher energy density. To combine the advantages of both fluids into one energy storage system, the hydro-pneumatic energy storage (HPES) system comes into being [16], which is an important idea in the studies of hybrid energy storage technologies [17-18].

The novel concept of HPES system is proposed and designed for the purpose of better system performance and smaller storage volume, and its basic working principle is shown in Fig. 1. In the pump mode (charging), water is pumped into pressure vessels and electricity power is converted to the pressure potential energy of air. In the turbine mode (discharging), the compressed air expands to expel water and the turbine is driven to produce electricity. A great number of studies on the HPES system are available. Energy and exergy characteristics of the HPES system were analyzed by Kim *et al*. and it is found that the quasi-isothermal compression/expansion processes are helpful to minimize the exergy loss [19-20], which exactly shows the difference between the Ericsson cycle and the Brayton cycle, and this quasi-isothermal process can be achieved by adjusting the polytropic exponent [21]. Thermodynamic and economic analyses of the HPES system with the salt cavern as a pressure vessel were conducted by Wang *et al*. and it is found that the HPES system has a high exergy efficiency (≈72.3%) while its economic performance should be improved by increasing the energy storage capacity (>2.4MW) [22-24]. Besides, the concept of HPES is employed to improve the power performance of the energy storage system in hybrid mining trucks [25]. Experimental studies of Buhagiar *et al*. at the University of Malta show that the HPES system exhibits excellent potential in the context of offshore wind and is ideal for mitigating the intermittency of wind energy. In particular, the enhanced heat exchange with the marine environment, acting as a natural heatsink, yields a quasi-isothermal condition, but its foundation is the service of efficient hydraulic machinery [26-28]. Theoretical analyses of Bi *et al*., Mozayeni *et al*. and Marefati *et al*. indicate that the pump is the most important component in the design and operation of HPES and the system performance can be significantly improved if the pump mode efficiency can be increased [29-31]. Experimental analyses of Yin *et al*. and Odukomaiya *et al*. further verify that most of the energy loss occurs in the pump mode and indicate that the hydraulic performance of the pump in the HPES system should be further investigated [32-33]. Moreover, an experimental study of an HPES system with a reversible centrifugal pump as the core equipment was performed by Sampedro *et al*. and it is found that the operating condition with a variable pressure in pump mode is a major challenge. Actually, the energy conversion instability caused by the pump experiencing off-design conditions can reduce the system efficiency and even affect the system safety. Although the best efficiency control or power control strategies worked in this model test [34-35], the problem of a variable operating condition in the pump mode has not been completely solved due to the complex non-linear relationship between the pressure change Δp and the system flowrate Q.

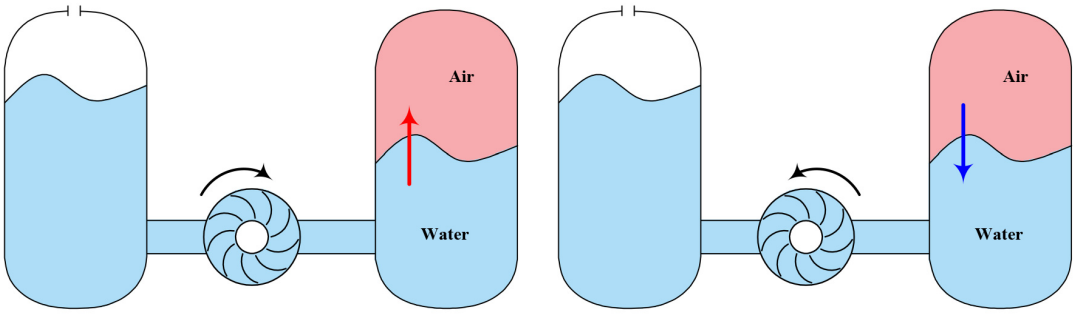

(a) Pump mode (charging) (b) Turbine mode (discharging)

Fig. 1. Basic working principle of the HPES system

The use of centrifugal pumps in the HPES system can minimize the development cost because they can be applied to a wide range of heads and flowrates and they are also the most widely used pump type in industrial applications [24,35-36]. It is proven that the working path of HPES can be close to an ideal isothermal cycle, and the temperature change of water during the compression and expansion processes is almost negligible, so the centrifugal pump can be regarded as working in the constant temperature water to pressurize the air. Because a single pump with a constant rotational speed is usually difficult to meet huge pressure changes in compressed air, the current pressurization strategy of HPES includes the relay pressurization [24] and the variable speed pressurization [32]. As shown in Fig. 2(a), the relay pressurization strategy is to use multiple centrifugal pumps with different head ranges for relay work. If the head of Pump-A reaches the set level (PA1→PA2), the Pump-A is stopped and the Pump-B is started to continue the energy storage process (PB1→PB2), and this operation is performed until the electricity power is no longer available or the maximum pressure level H_{max} is reached. Obviously, a single pump in this pump group will experience variable operating conditions. As shown in Fig. 2(b), the variable speed pressurization strategy is to change the rotational speed of centrifugal impeller to meet the boundary pressure rise. For a certain pipeline system, the required head may increase as the rotational speed increases. Under this condition, the flowrate Q has a little change, but the pump still experiences greatly variable operating conditions (PN1→PN2→PN3) according to the similarity laws [37]. In contrast, the second strategy may have a smaller variable range and it is more conducive to the pump operating in the high efficiency zone. However, the required variable speed range determines the complexity of such power conversion equipment as inverters, variable frequency drives and other auxiliary components. All of these are included in the cost budget and may be very expensive [28], so it is still of both technological and economic significance to study the energy conversion characteristics of the pump mode in a wide variable operating range. In addition, this problem may also exist in the PHES system, especially in the case of low head and large water level changes [38], and thus the relevant studies of hydro-energy machinery can provide valuable references.

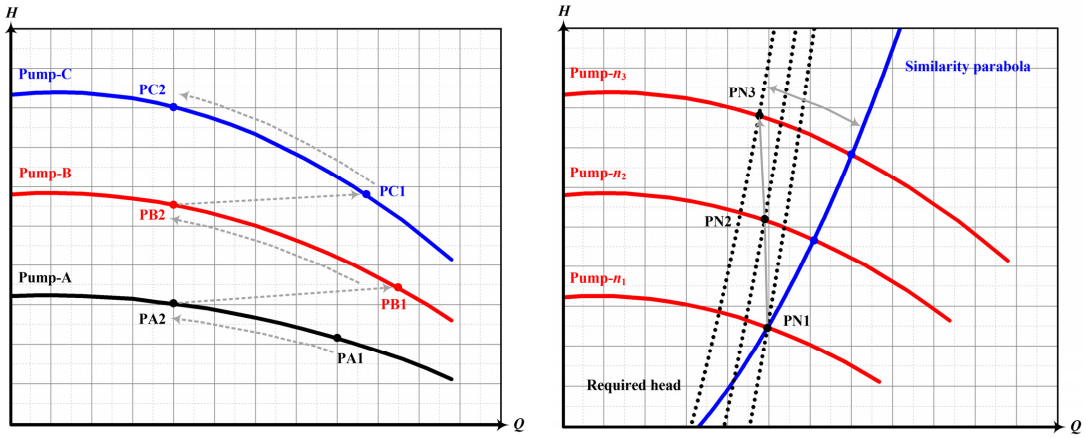

(a) Relay pressurization strategy (b) Variable speed pressurization strategy

Fig. 2. Variable operating conditions in the pump mode

Energy conversion instability caused by the pump experiencing off-design conditions is mainly due to inner flow instability, and a great number of studies on this topic are available. Experimental and numerical simulation studies on a reversible storage pump (or pump-turbine) were performed by Li *et al*. and it is found that the hysteresis phenomenon in the hump region of flowrate-head curve is caused by the backflow at the impeller inlet and the separation vortices in the guide-vane domain

[39-41]. Experimental and numerical simulation studies on the double humps of a reversible storage pump were conducted by Luo *et al*. [42-43] and Wang *et al*. [44-45], and it is found that the two hump regions with positive slopes are induced by two different stall flows, which correspond to the separation change at the blade inlet and the stall change in the guide-vane domain, respectively. Experimental and numerical simulation studies on the flowrate-head curve instability of a single-stage centrifugal pump were carried out by Li *et al*. and it is found that the backflow at the impeller inlet and the counter-rotating vortices at the impeller outlet lead to a drastic increase in the entropy generation rate [46], which is the main cause of this instability. The rotating stall characteristics in a centrifugal pump with/without vaned diffuser were analyzed by Feng *et al*. and it is found that the existence of the hump region is closely related to the presence of guide vanes and a reasonable number of guide vanes greatly suppresses pressure fluctuations in the vaneless region [47]. Besides, the evolution of inner flows during the shutdown process of a reversible storage pump was analyzed by Wang *et al*. and such transient characteristics as pressure fluctuation and torque pulsation in this progressive process are preliminarily presented and quantified [48]. Actually, for the transient flow evolution in a centrifugal pump during the startup and shutdown processes, Bois *et al*. and Wu *et al*. also conducted the similar theoretical and numerical simulation studies [49-51]. Moreover, to clarify the hydrodynamics of the reversible centrifugal pump operating at off-design conditions, high-speed flow visualizations of rotating stall in the guide-vane domain were carried out by the Laboratory for Hydraulic Machines in EPFL and the propagation process of stator stall cells is clearly revealed [52-53]. The PIV (particle image velocimetry) test in the double hump region of a reversible centrifugal pump was carried out in Dongfang Electric Machinery Co. Ltd. and the complex vortical structures corresponding to different operating points are well captured [54]. On the whole, there are many valuable results on the off-design performance of pump mode in the PHES system, which are similar to the study on compressor mode in CAES system [55-56]. However, this is not enough for us to fully understand the aforementioned energy conversion instability of pump mode in HPES system (Fig. 2). On the one hand, the above studies mainly focus on the operating condition of a centrifugal pump with significantly unstable flows (e.g. the hump or saddle zone), but it is yet to systematically summarize the evolution of the energy conversion instability and the corresponding flow events, which is not conducive to tracking the deterioration process of the energy performance. On the other hand, the current research has not yet proposed an effective criterion for guiding the determination of the design operation limit (or the stability limit [57]) of the pump mode, which is not conducive to the formulation of a reasonable pressurization strategy.

In this paper, the experimental and numerical simulation investigations of a centrifugal pump with vaned diffuser will be further conducted in a wide operating range, with the aim of achieving the following two sub-objectives:

1) To systematically analyze and summarize the evolution process of the energy conversion instability and the corresponding flow events.

2) To propose an effective criterion for determining the stability limit of pump mode based on the above analysis of inner flow characteristics.

The study processes of this article are organized as follows. In Sec. 2, the experiment of energy performance is performed and the phenomenon of energy conversion instability is presented. In Sec. 3, the numerical simulation scheme and its validation are conducted. In Sec. 4, the evolution stage of this instability, the corresponding energy budget characteristics and the development of energetic vortical structures are successively discussed. In Sec. 5, the conclusions are given.

2 Experiment of energy conversion characteristics

The following features are available for the centrifugal pump working in HPES system: (1) the temperature change in the water during the charging processes is almost negligible, and the pump can be regarded as working in the constant temperature water to pressurize the air; (2) the charging time can be as long as several hours for both pressurization strategies, so the operating condition is changed in a quasi-steady manner; (3) both pressurization strategies can be simplified to the variable operating condition of a single pump with a constant rotational speed according to the similarity law. Accordingly, it is reasonable and feasible to directly study the energy conversion characteristics caused by the head change of a single pump.

As shown in Fig. 3, a single-suction centrifugal pump model with vaned diffuser is used in this study, and the energy performance test was conducted by using the hydraulic machinery test rig in China Institute of Water Resources and Hydropower Research [58-59], and the total uncertainty of the model efficiency is ±0.2%. Moreover, the pump impeller diameter D_2 is 450 mm, and the rotor blade number Z is 7. The rated head H_0 is 21.78m, the rated flowrate Q_0 is 116.61L/s, the rated rotational speed n is 900r/min, and the specific speed n_s ($nQ_0^{0.5}/H_0^{0.75}$) is approximately 30.48.

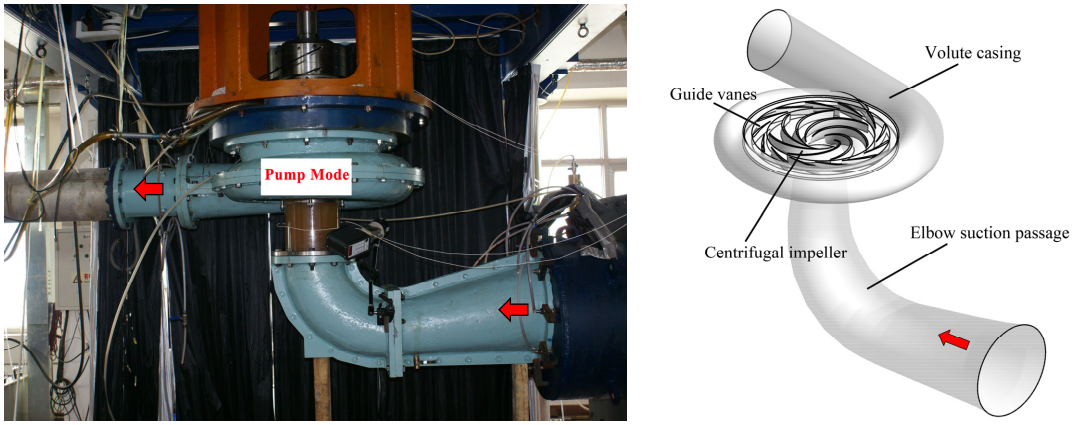

(a) Experimental setup of the storage pump (b) Structures of the storage pump

Fig. 3. Performance test of a centrifugal pump with vaned diffuser

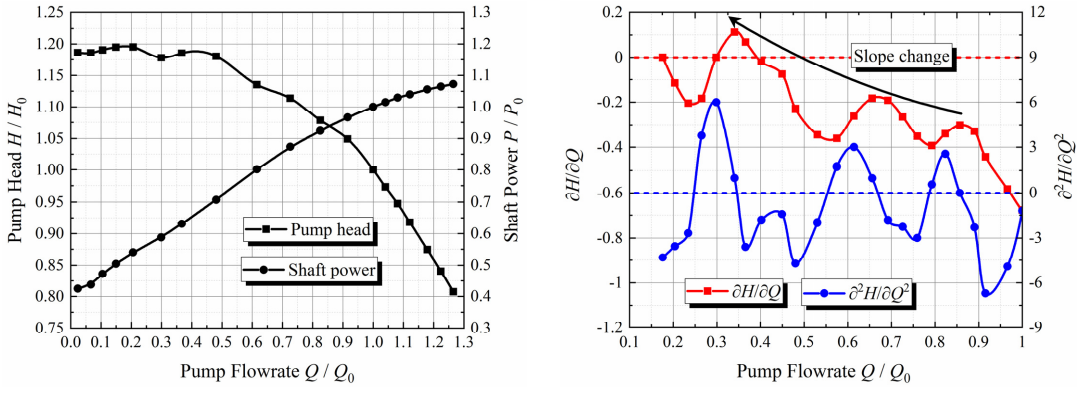

(a) Performance curves (b) Slope change of the head-flowrate curve

Fig. 4. Experimental results of the energy conversion characteristics

The pump head-flowrate curve (H-Q) and the shaft power-flowrate curve (P-Q) are shown in Fig. 4(a). With the increase of pressure ratio H/H_0, the phenomenon of energy conversion instability is observed. For this unsmooth head curve, the distributions of the first-order derivative $\partial H/\partial Q$ and the second-order derivative $\partial^2 H/\partial Q^2$ are shown in Fig. 4(b). The slope $\partial H/\partial Q$ increases in a bumpy

way as the pressure ratio H/H_0 rises, and a positive slope (the hump or saddle zone) appears when Q/Q_0<0.4. In this process, the concavity/convexity $\partial^2 H/\partial Q^2$ also significantly changes. This graded feature indicates that the instability has a progressive process, but the above data are not enough to clearly determine the development stage, and the evolution of inner flow patterns should be further analyzed by numerical computation, especially for the operating conditions of Q/Q_0<1.

3 Numerical simulation scheme and flow analysis method

3.1 Numerical simulation scheme and its validation

A time-scale-driven hybrid URANS/LES model for rotating turbulence is utilized to simulate the flow fields in centrifugal pump, which was developed by the authors and is referred to as *TSD* model. The TSD model is characterized by a time-scale-driven damping function of the turbulent viscosity and has been proven to enable efficient computations of turbulent flow and cavitating flow in hydro-energy machinery [60-61]. On the basis of it, high quality hexahedral grids are employed to discretize the computational domains shown in Fig. 3(b). The boundary layer meshing of rotor blades and stator vanes is taken into account, and other regions with complex geometry are also locally refined. To guarantee the reliability of numerical computations, the GCI criterion that is based on the Richardson extrapolation method and recommended by ASME is used for the grid convergence analysis, and the details are given in the *Appendix A*. As shown in Fig. 5, the meshing scheme with 6,216,526 elements and 6,184,366 nodes is finally determined.

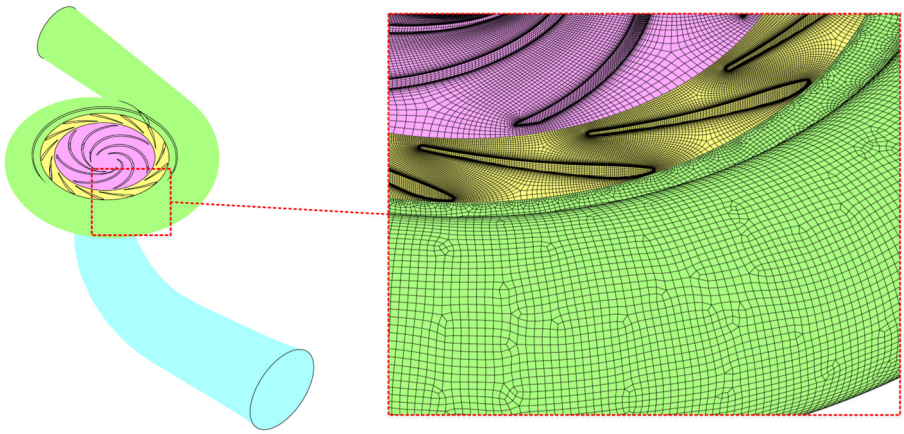

Fig. 5. Spatial discretization of the computation domain

Transient simulation assignments are conducted by using ANSYS CFX, and the time step δt is chosen as 1.8519×10^{-4}s to ensure that the RMS Courant number is less than 2. The discretization schemes of the transient term, convective term and the diffusion term are the second-order backward Euler scheme, the second-order upwind scheme and the central difference scheme, respectively. For the boundary conditions, the velocity inlet with a medium turbulence intensity is employed, and the pressure outlet is adopted. A no-slip condition is used for wall surfaces, and the convergence residual standard is set to 1.0×10^{-5}. As shown in Fig. 6(a), the time-weighted average results of *H-Q* and *P-Q* are obtained based on the above simulation scheme. The relative error of the pump head *H* is less than 2.5% within the range of $0.2Q_0$~$1.0Q_0$, and the relative error of the shaft power is less than 5.1%. A comparison of the peak-to-peak value (PPV) $\Delta H/H$ of pressure fluctuations in the vaneless region is shown in Fig. 6(b), and the relative error of it is less than 1.81% within the range of $0.6Q_0$~$1.0Q_0$. Accordingly, this proves that the transient simulation results are in good agreement with that of the experiment [58], and the numerical computation in this study is trustworthy.

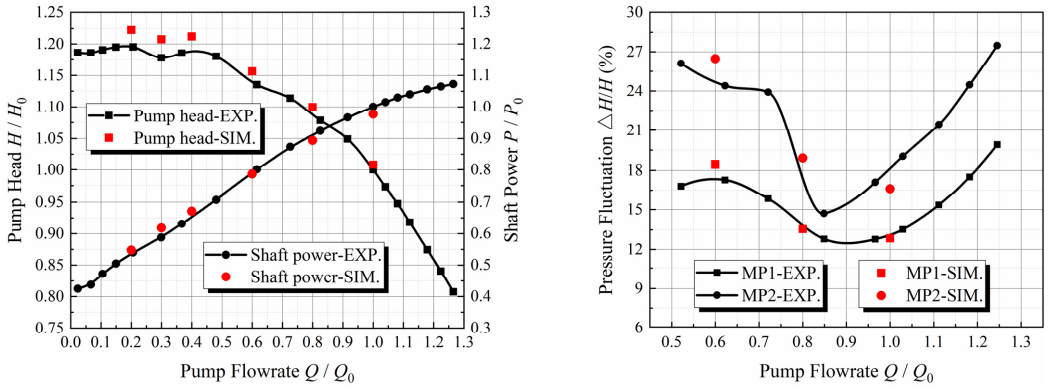

(a) Performance curves (b) PPV of pressure fluctuations

Fig. 6. A comparison of the experimental results and the simulation results

3.2 Diagnostic method of flow instability in centrifugal pump

The relative momentum equation of incompressible flows in a centrifugal pump impeller can be expressed as [59]

$$\boldsymbol{V}_r \cdot \nabla \boldsymbol{V}_r = -\nabla I_p - 2\boldsymbol{\omega}_i \times \boldsymbol{V}_r \tag{1}$$

where $\boldsymbol{V}_r$ is the relative velocity vector, $I_p=p/\rho-\omega_i^2 r^2/2$ is referred to as potential rothalpy, and $\boldsymbol{\omega}_i$ is the rotor angular velocity vector. This equation implies that the macroscopic flow pattern in a blade channel of an impeller is driven by the potential rothalpy gradient (PRG) and the Coriolis force, and PRG has an active control effect. The ideal flow pattern in a centrifugal pump impeller should be one where the fluids uniformly flow out along the blade profile. Under this condition of curvilinear motion with a uniform speed, it is the PRG that actively adjusts the Coriolis force so that the motion trajectory of the fluids conforms to the blade profile. To reflect this essential flow characteristic in a centrifugal pump impeller, a dynamic expression of the blade profile differential equation was proposed by the authors and is given by [62]

$$\begin{cases} F_n = \rho \left\| -2\boldsymbol{\omega}_i \times \boldsymbol{V}_r - \nabla I_p \right\|_2 \\ r^* \sqrt{\dfrac{F_n}{\rho r^*}} = \sqrt{F_n r^* / \rho} = \left\| \boldsymbol{V}_r \right\|_2 \\ \left\langle \boldsymbol{F}_n, -\boldsymbol{r} \right\rangle = \beta \end{cases} \tag{2}$$

where $\boldsymbol{F}_n$ is centripetal force of the curvilinear motion, ρ is the density, r^* is the curvature radius of local blade profile, and β is the relative flow angle. As shown in Fig. 7, the blade profile can be regarded as the integral curve of the differential motion trajectory induced by the centripetal force $\boldsymbol{F}_n$, and the included angle between $\boldsymbol{F}_n$ and the position vector $-\boldsymbol{r}$ is exactly the relative flow angle β. Accordingly, for the backward-swept impeller (β_2<90°) [37], a necessary condition for the fluids stably moving along a given blade profile is that the magnitude of PRG is smaller than that of the Coriolis force $\boldsymbol{F}_C$. Hence, a general diagnostic function SI of flow instability in a centrifugal pump impeller was proposed by the authors and can be expressed as [62]

$$SI = \frac{|\mathrm{PRG}|}{|\boldsymbol{F}_C|} = \frac{\left\| -\nabla I_p \right\|_2}{\left\| -2\boldsymbol{\omega}_i \times \boldsymbol{V}_r \right\|_2} \tag{3}$$

In theory, large-scale vortical structures with the features of local low pressure, low velocity and high pressure gradient appear with the development of separation flows, and the diagnostic function *SI* is much greater than 1 in these regions. For different geometric structures and inflow conditions, the diagnostic function *SI* can provide a clear and uniform diagnostic criterion. Besides, the PRG is directly related to the rotor blade loading δp, so *SI* is also the bond that establishes the relationship of "vortex characteristics↔PRG distributions↔blade loading↔energy conversion characteristics".

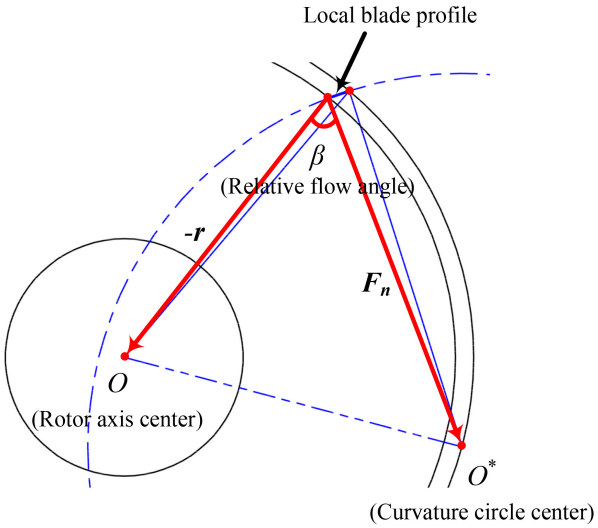

Fig. 7. Dynamic expression of the blade profile differential equation

4 Evolution process of energy conversion instability

4.1 Analysis of the evolution stage

The energy conversion instability of pump mode is presented in Fig. 4(b), and the quantitative description of its evolution stage should be based on the flow characteristics in the impeller domain. The average values of the diagnostic function *SI* at the blade channel inlet and the standard deviation of the meridian velocity C_m at the blade channel outlet are shown in Fig. 8. The former is defined as the spatio-temporal average values of the diagnostic function SI_1 of all inlet monitor points (see *Appendix B*), which characterizes the inflow stability. The latter is defined as the time-weighted average values of the standard deviation of the spatially-weighted average values of the meridian velocity C_{m2} at each blade channel outlet, which characterizes the outflow uniformity.

According to the STD(C_{m2})-Q curve in Fig. 8, it is found that the outflow uniformity constantly decreases as the pressure ratio H/H_0 increases, especially for the operating conditions of $Q/Q_0<0.6$, and this curve fits well with the exponential function form of $f(Q)=a\cdot b^{Q}+c$. This implies that the outflow imbalance of each blade channel in the impeller domain rapidly increases as the pressure ratio H/H_0 increases, which also reflects the growth of the relative blockage in blade channels, and it is exactly the sign of stall [62-63]. According to the AVG(*SI*)-Q curve in Fig. 8, the diagnostic function *SI* at the blade channel inlet has little change in the process of $1.0Q_0\rightarrow0.8Q_0$, and the PRG is approximately 0.6 times the magnitude of the Coriolis force. When the flowrate is lower than $0.8Q_0$, the *SI* rapidly increases until it reaches the critical value 1 (blue chain line in Fig. 8) at the condition of $0.64Q_0$, and it implies that the inflow stability is irreversibly damaged. The *SI* keeps increasing as the flowrate further decreases. According to the above diagnosis of flow patterns, the energy conversion of pump mode shows three typical stages: (1) Good inflow stability is presented for $Q/Q_0\in[0.8,1.0]$. The inner flow is in the stage of *stall-free* ($SI\approx0.6$) and the corresponding head

curve is in a stable negative slope zone, so the energy conversion is in the stage of *stable work*; (2) The inflow stability is irreversibly damaged for $Q/Q_0 \in [0.64,0.8]$. The inner flow is in the stage of *stall inception* ($SI \rightarrow 1$) and the corresponding head curve shows an instability trend, so the energy conversion is in the stage of *stumbled work*; (3) The inflow stability becomes increasingly worse for the operating conditions of $Q/Q_0<0.64$. The inner flow is in the stage of *stall deepening* ($SI>1$) and the corresponding head curve shows a significant instability, so the energy conversion is in the stage of *shaky work*. Due to the generality of the diagnostic function SI, this AVG(SI)-Q curve should show a general evolution process for the energy conversion characteristics of pump mode.

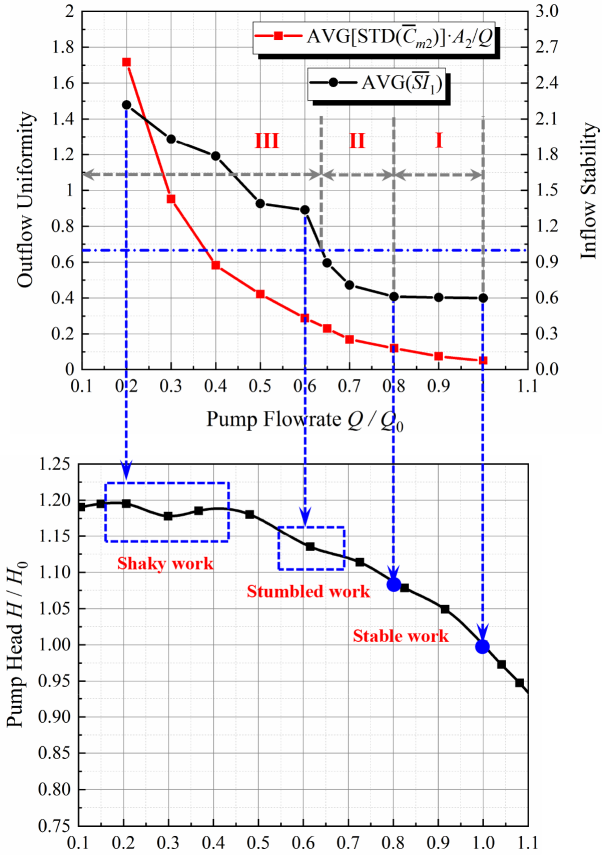

Fig. 8. Evolution stage of the energy conversion instability

4.2 Analysis of the energy budget

The rotor blade loading δp is the dynamic source of pump work or energy income, which is the static pressure difference between the impeller blade pressure and suction surfaces. The streamwise distributions of the time-weighted average values of the potential rothalpy I_p in the impeller domain under six typical operating conditions are shown in Fig. 9, which correspond to the above evolution stage (Fig. 8). In addition, because the time-weighted average values of I_p at the monitor points in each blade channel are almost the same after the long-period transient simulations, the results in the blade channel ① (see Fig. B. 1(a)) are analyzed here, and the original naming form of the monitor points is simplified as "IP" + "blade channel position 1" + "spanwise position s" + "circumferential position θ" (see *Appendix B*).

Under the $1.0Q_0$ condition, the potential rothalpy I_p on the inlet shroud side ($s \rightarrow 1$) is much lower than that on the inlet hub side ($s \rightarrow 0$), and then the I_p on the hub side is slowly increased while the I_p on the shroud side is quickly increased. At the middle part of the blade channel, the I_p on the

hub side has a little change. At the aft part of the blade channel (l>0.8), the difference in I_p between the shroud and hub sides is rapidly reduced and its values tend to be the same. This distribution of I_p is consistent with the theoretical blade loading strategy [59] and can ensure the good capability of energy conversion. Under the $0.8Q_0$ condition, the curve slope near the blade channel inlet ($0 \leqslant l \leqslant 0.2$) increases, especially on the inlet shroud side, and it causes an overall decrease in the blade loading δp or the impeller torque M_l. Under the $0.6Q_0$ condition, the streamwise distributions of I_p have significantly changed, and the curve slope near the blade channel inlet ($0 \leqslant l \leqslant 0.2$) rapidly increases, which implies that the natural adverse PRG in this area is constantly increasing. The work ability on the inlet shroud side is almost lost ($\delta p \to 0$), and the blade loading at the middle and aft parts is also significantly reduced. Under the $0.4Q_0$ condition, the distribution of I_p becomes worse. The curve slope on the inlet shroud side ($s \to 1$) and the hub side near the blade suction surface ($s \to 0$ and $\theta \to 1$) further increases, and the blade loading at the middle and aft parts is further reduced. Besides, at the blade channel outlet ($l \to 1$), the reduction of the I_p-l curves is significantly reduced, and the I_p values on the blade pressure surface and the blade suction surface no longer tend to be the same. Under the $0.3Q_0$ and $0.2Q_0$ conditions, the distributions of I_p become increasingly worse, and the area originally responsible for important work tasks has lost a lot of work ability. At the aft part of the blade channel (l>0.8), the reduction of the I_p-l curves is further reduced, which implies that the static pressure in this area is constantly increasing, and the I_p value near the blade pressure surface is much greater than that near the blade suction surface, especially on the outlet hub side. On the whole, in the above evolution process of the energy conversion instability in pump mode (Fig. 8), the attenuation of rotor blade loading δp gradually spreads from the inlet shroud side to the entire blade, which is the source affecting energy income and inducing flow instability.

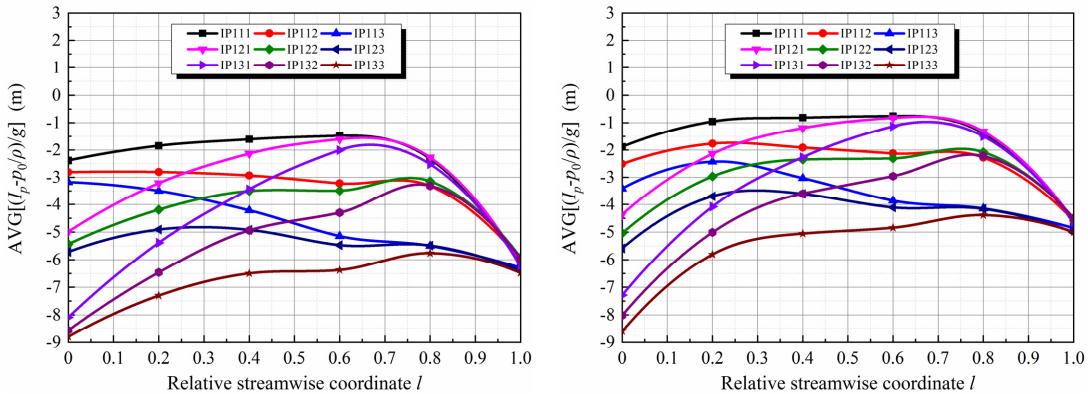

(a) Q/Q_0=1.0 (b) Q/Q_0=0.8

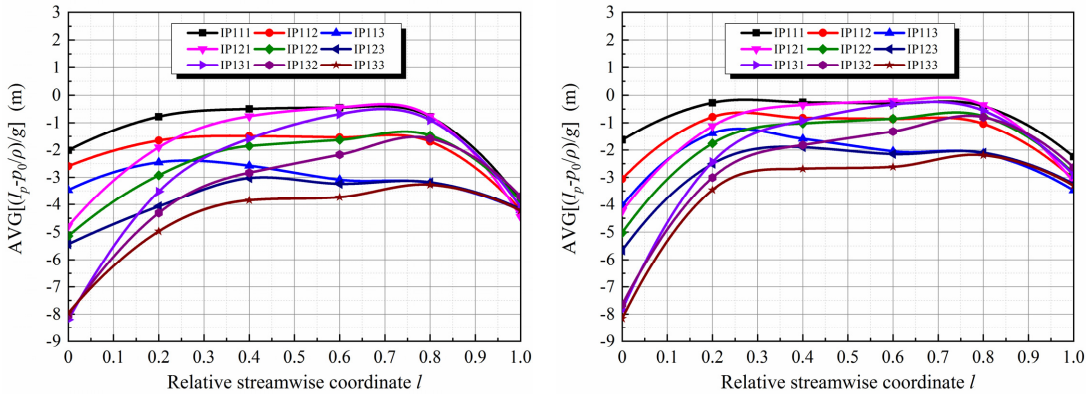

(c) Q/Q_0=0.6 (d) Q/Q_0=0.4

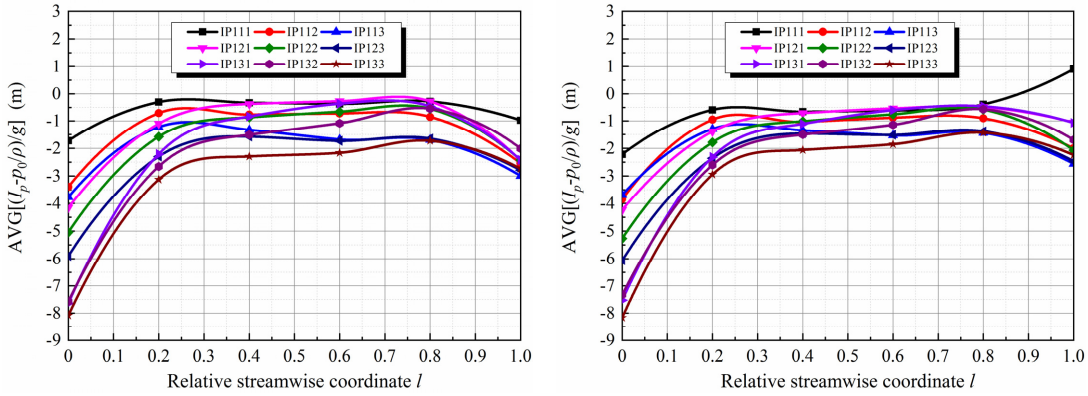

(e) Q/Q_0=0.3 (f) Q/Q_0=0.2

Fig. 9. Streamwise distributions of the potential rothalpy I_p

A comparison of the energy conversion characteristics under different operating conditions is shown in Fig. 10. Note that the energy signal characterized by the total pressure in the absolute coordinate system is expressed in the form of water column height (in meters), and the energy gates 1~5 correspond to the elbow suction passage inlet, the centrifugal impeller domain inlet, the guide-vane domain inlet, the volute casing inlet and the volute casing outlet, respectively. Under the $1.0Q_0$ condition, the shaft power $M_I\omega_i/\rho gQ$ and the total pressure signal at each energy gate have a stable wave character and low amplitude, and the relative magnitude between the hydraulic loss δh (the total pressure drop between the adjacent energy gates) and the shaft power is small. This is direct evidence that the energy conversion is in the stage of *stable work* (Fig. 8). Under the $0.8Q_0$ condition, the wave characters of these energy signals are still stable while slight disturbances can be observed, especially in the shaft power curve, and the hydraulic loss δh of annular cascade regions increases. Under the $0.6Q_0$ condition, the energy signals of the shaft power and the total pressure at each energy gate become unstable and have larger amplitudes, and the hydraulic loss δh rapidly rises. This also corresponds to the fact that the energy conversion is in the stage of *stumbled work* (Fig. 8). Under the $0.4Q_0$ condition, the wave characters of these energy signals become more disordered and the amplitudes further increase, while some low-frequency components are already visible. Besides, the hydraulic loss δh of annular cascade regions significantly rises, and the δh of the elbow suction passage can no longer be ignored. Under the $0.3Q_0$ and $0.2Q_0$ conditions, the energy signals become increasingly worse, and the wave characters with high amplitude and significant low-frequency components are presented. The average value of shaft power (energy income) is almost 3 times that

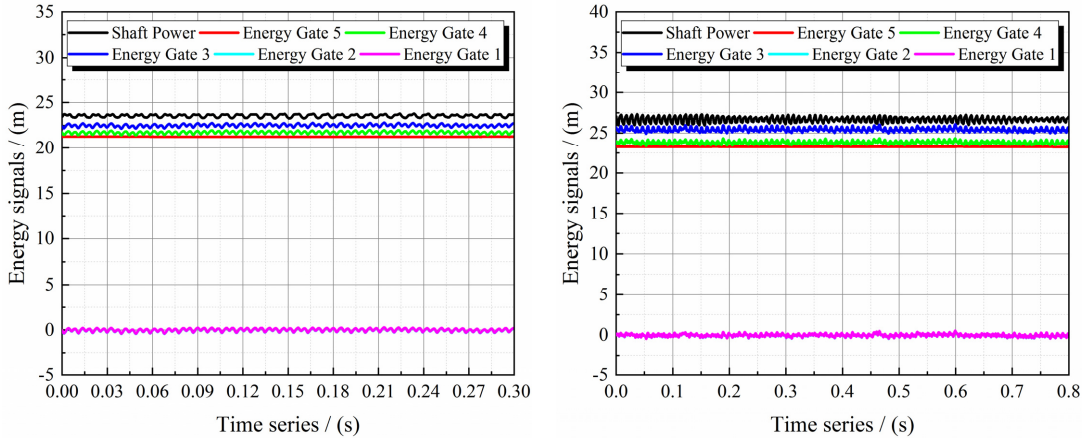

(a) Q/Q_0=1.0 (b) Q/Q_0=0.8

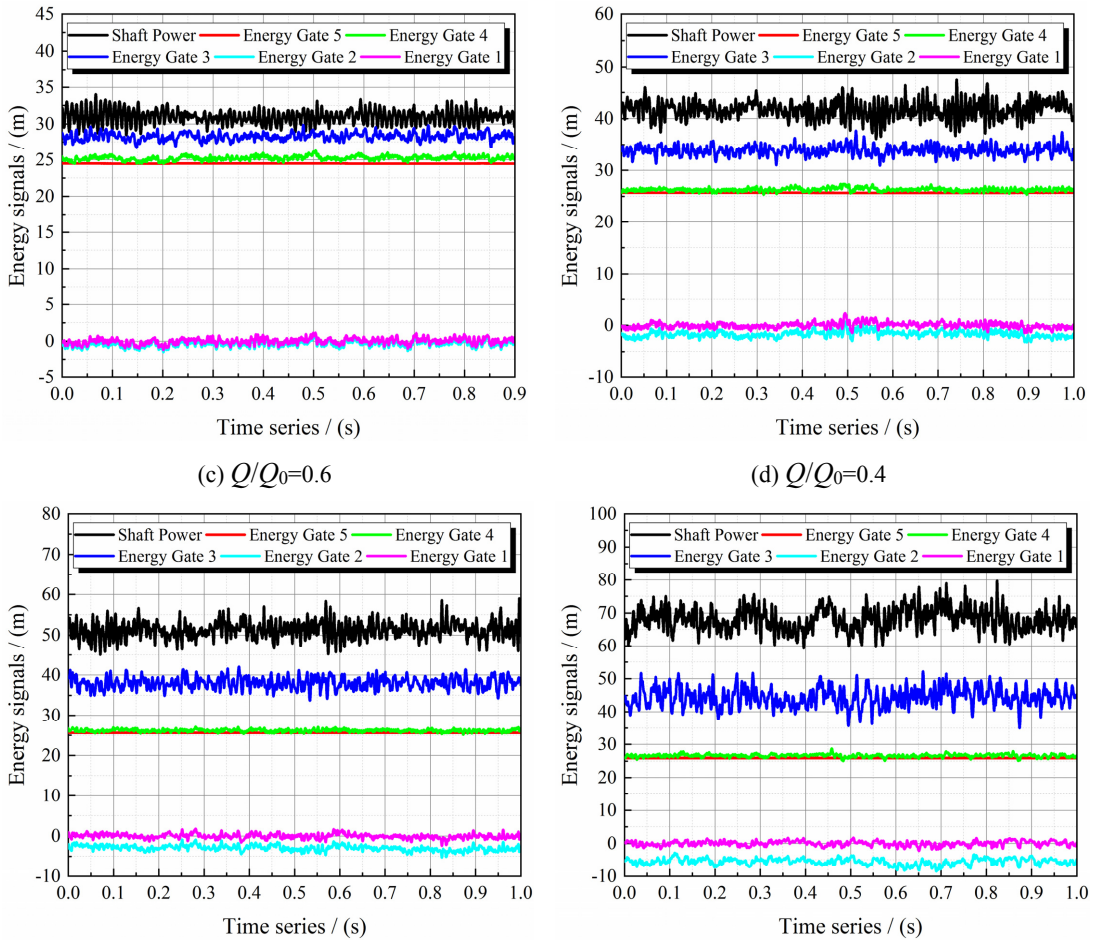

(c) Q/Q_0=0.6 (d) Q/Q_0=0.4

(e) Q/Q_0=0.3 (f) Q/Q_0=0.2

Fig. 10. Energy income and expenditure under different operating conditions

of the 1.0Q_0 condition, but the majority of it is dissipated in the flow passages (energy expenditure), which is the source of high entropy production [39,64]. These features correspond to the fact that the energy conversion is in the stage of *shaky work* (Fig. 8).

A quantitative growth model of the energy conversion instability is obtained according to the above energy budget analysis. As shown in Fig. 11(a)~(b), for the shaft power P and the pump head H, the two PPV-Q curves fit well with the Logistic S-function form of $f(Q)=a+b/(1+(Q/c)^d)$, which can be regarded as a special power law growth model. Within the range of $Q/Q_0 \in [0.8,1.0]$, the fluctuation amplitudes of the shaft power and the pump head slowly increase as the pressure ratio rises, and the increments of $\Delta P/P$ and $\Delta H/H$ are 2.72% and 0.81%, respectively. Within the range of $Q/Q_0 \in [0.5,0.8]$, the fluctuation amplitudes of the shaft power and the pump head rapidly increase as the pressure ratio rises, and the increments of $\Delta P/P$ and $\Delta H/H$ are 22.32% and 8.3%, respectively. During this period, the maximum curve slope or change rate occurs approximately at the operating condition of Q/Q_0=0.64, which is a typical sign of the instability development. Within the range of $Q/Q_0 \in [0.2,0.5]$, the change rates of $\Delta P/P$ and $\Delta H/H$ slow down quickly, and their increments are 2.54% and 1.79%, respectively. Obviously, this growth model is well consistent with the evolution features determined by the diagnostic function SI, especially for the critical operating condition. The stability is irreversibly damaged if $SI>1$, and the resultant hydraulic efficiency drop and pressure fluctuation surge can affect the safe and stable operation, which should be avoided as much as possible. Accordingly, the critical condition for the energy conversion instability is the

diagnostic function *SI*=1, and this can be an effective criterion for determining the stability limit in pump mode. Besides, the proportions of the hydraulic loss δh in the impeller head H_i in each domain are shown in Fig. 11(c). As the pressure ratio rises, the hydraulic loss ratio $\delta h/H_i$ increases in a cubic power law, and the annular cascade regions are always the major "disaster area". The $\delta h/H_i$ in the elbow suction passage is almost negligible when *SI* is less than 1, while it significantly increases when *SI* is greater than 1, which implies the existence and development of special flow events in the above evolution process of energy conversion instability.

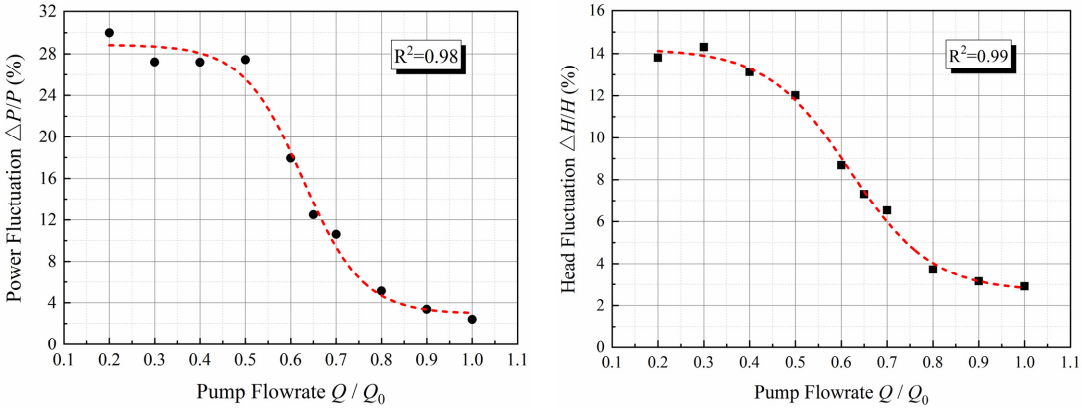

(a) PPV of shaft power fluctuations

(b) PPV of pump head fluctuations

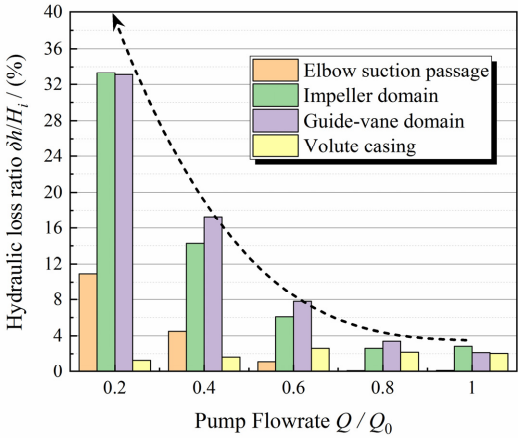

(c) Distributions of the hydraulic loss ratio

Fig. 11. Growth model of the energy conversion instability

4.3 Analysis of the energetic vortical structures

To further understand the typical flow events in the evolution process, the vortical behavior of energetic vortical structures in the impeller domain should be analyzed. According to the vorticity decomposition theory, the classical vorticity $\boldsymbol{\omega}$ (velocity curl) can be decomposed into the rigid vorticity $\boldsymbol{\omega_R}$ and the deformational vorticity $\boldsymbol{\omega_S}$, and the swirling features of a vortex are mainly determined by the rigid vorticity because it exactly represents the rigid rotation motions of local fluids [65-66]. The explicit expression of the rigid vorticity is given by [66]

$$\begin{cases} \boldsymbol{\omega} = \nabla \times \boldsymbol{V} = \boldsymbol{\omega_R} + \boldsymbol{\omega_S} \\ \boldsymbol{\omega_R} = \left[\boldsymbol{\omega} \cdot \boldsymbol{r} - \sqrt{(\boldsymbol{\omega} \cdot \boldsymbol{r})^2 - 4\lambda_{ci}^2} \right] \cdot \boldsymbol{r} \end{cases} \tag{4}$$

where $\boldsymbol{\omega}$ is the total vorticity (velocity curl), $\boldsymbol{\omega_R}$ is the rigid vorticity, $\boldsymbol{\omega_S}$ is the deformational vorticity,

$\boldsymbol{r}$ is the real eigenvector of the velocity gradient tensor (or the direction vector of the rigid rotation axis), and λ_{ci} is the imaginary part of complex conjugate eigenvalues of the velocity gradient tensor. It has been proved that this new physical quantity can provide a practical method for the analysis and control of vortical flows in hydro-energy machinery [62,67].

The streamwise distributions of the time-weighted average values of the rigid vorticity $\|\boldsymbol{\omega_R}\|_2$ in the impeller domain under six typical operating conditions are shown in Fig. 12, corresponding to the above evolution stage (Fig. 8). Under the $1.0Q_0$ condition, the average values of rigid vorticity in the blade channels are lower than $2\omega_i$ (ω_i is the rotor angular velocity) and show a downward trend along the streamwise direction. Under the $0.8Q_0$ condition, the distribution trend is close to that of the $1.0Q_0$ condition, and most of the average values of rigid vorticity in the blade channels are still lower than $2\omega_i$. Under the $0.6Q_0$ condition, the streamwise distributions of rigid vorticity have a significant change, and its maximum value is greater than $3\omega_i$. At the fore part of the blade channel ($0 \leqslant l \leqslant 0.2$), the swirling strength on the shroud side ($s \rightarrow 1$) increases. At the aft part of the blade channel ($0.8 \leqslant l \leqslant 1$), the trend of swirling strength surge is presented, especially in the region close to the blade pressure surface ($\theta \rightarrow 0$). This indicates that energetic vortical structures appear at the impeller inlet and outlet, which is also related to the changes of blade loading (Fig. 9(c)). Under the $0.4Q_0$ condition, the maximum value of rigid vorticity is greater than $5\omega_i$. The above surge near the inlet shroud and the outlet pressure surface is strengthened, and the swirling strength on the inlet hub side ($s \rightarrow 0$) also increases. This describes the growing vortical structures and corresponds to the change trends of the above energy signals (Fig. 9(d) and Fig. 10(d)). Under the $0.3Q_0$ and $0.2Q_0$ conditions, the spatial features of the relatively high swirling strength near the blade channel inlet and outlet while the relatively low swirling strength at the middle part become clearer. Meanwhile,

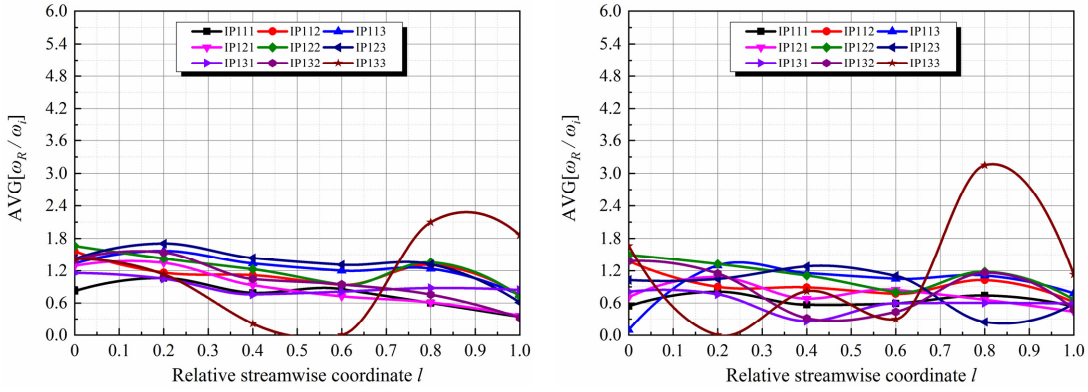

(a) Q/Q_0=1.0 (b) Q/Q_0=0.8

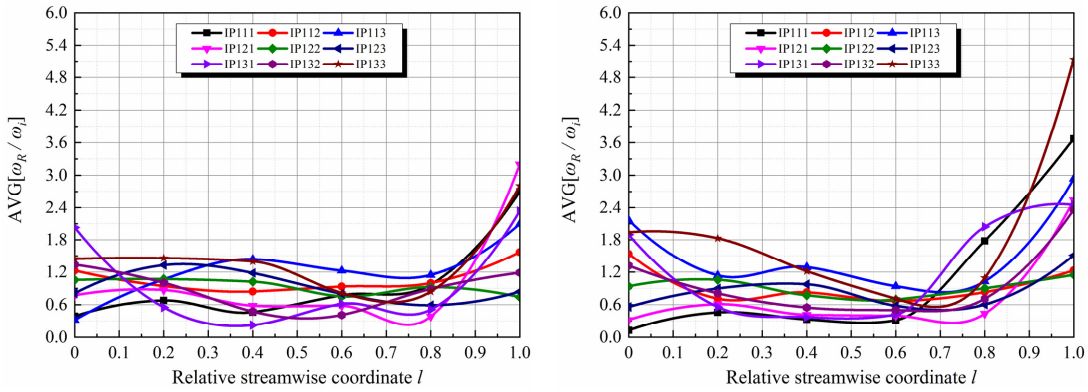

(c) Q/Q_0=0.6 (d) Q/Q_0=0.4

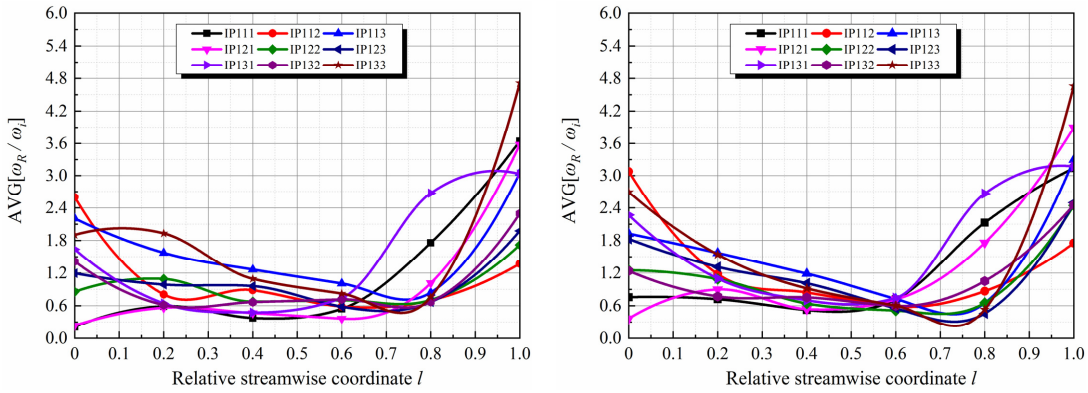

(e) Q/Q_0=0.3 (f) Q/Q_0=0.2

Fig. 12. Streamwise distributions of the rigid vorticity $\|\boldsymbol{\omega_R}\|_2/\omega_i$

the high swirling strength range near the blade channel inlet and exit is gradually widened, reflecting that the energetic vortical structures are developing to become increasingly stronger in the *stall deepening* process (or the *shaky work* stage in Fig. 8).

The time-averaged streamline distributions at different evolution stages are shown in Fig. 13. The average motion is the first focus of engineering turbulence and directly reflects the nature of macroscopic flow characteristics. At the stage of *stall-free*, the streamlines in the blade channel are smooth and fit well with the blade profile. The diagnostic function *SI* is approximately 0.6, and this good flow pattern without large-scale vortical structures ensures the performance of *stable work*. At the stage of *stall inception* (*SI*→1), the backflow trend appears on the inlet shroud side, while the helical vortex trend appears on the outlet pressure surface side. This flow pattern change is a vivid description of the above rigid vorticity distribution (Fig. 12(c)) and can be regarded as the result induced by the aforementioned blade loading attenuation. At the stage of *stall deepening* (*SI*>1), the backflow trend has developed into the large-scale backflow vortices, while the helical vortex trend has developed into the large-scale streamwise helical vortices. These energetic vortical structures occupy large areas at the blade channel inlet and outlet, while the middle part is a weak separation zone with low velocity and low swirling strength (Fig. 12(f)). In particular, the leading backflow vortices and trailing helical vortices are the dominant vortical structures in the centrifugal impeller domain, which are further shown in Fig. 14(a)~(b). The leading backflow vortex originates from the *H*→*S* secondary flows induced by the natural adverse PRG on the S2 streamsurfaces [59], and this effect is gradually strengthened as the pressure ratio increases, thereby causing a rapid drop in blade loading on the inlet shroud side (Fig. 9), and the leading flow spillage comes into being and becomes a typical flow event where the swirling strength rises. The leading backflow vortices can develop into the elbow suction passage, greatly increasing the energy dissipation, and it corresponds to the phenomenon that the hydraulic loss ratio $\delta h/H_i$ in the elbow suction passage significantly increases if *SI* is greater than 1 (Fig. 11). The trailing helical vortex originates from the *P*→*S* secondary flows induced by the natural adverse PRG on the S1 streamsurfaces [59], and this effect is also gradually strengthened as the pressure ratio increases, thereby causing the worse work ability at the aft part, and the trailing helical vortex comes into being and also becomes a typical flow event where the swirling strength rises. The trailing helical vortices can develop into the guide-vane domain, greatly increasing the energy dissipation, and it corresponds to the phenomenon that the hydraulic loss ratio $\delta h/H_i$ in the annular cascade regions significantly increases with *SI* greater than 1 (Fig. 11). These two flow events are similar to those in the spike-type compressor stall [63,68]. Besides, the dynamic

stall cells can be observed on the inlet hub side [62], but the propagation characteristics are complex and will not be discussed in this study. Moreover, the power spectral density (PSD) distributions of rigid vorticity at the feature points in the leading/trailing vortical zones are shown in Fig. 14(c)~(d). At the regions with higher frequencies, the three-dimensional frequency spectra of rigid vorticity follow a -11/3 scaling law in a wide range, while the frequency spectra of the shaft power and pump

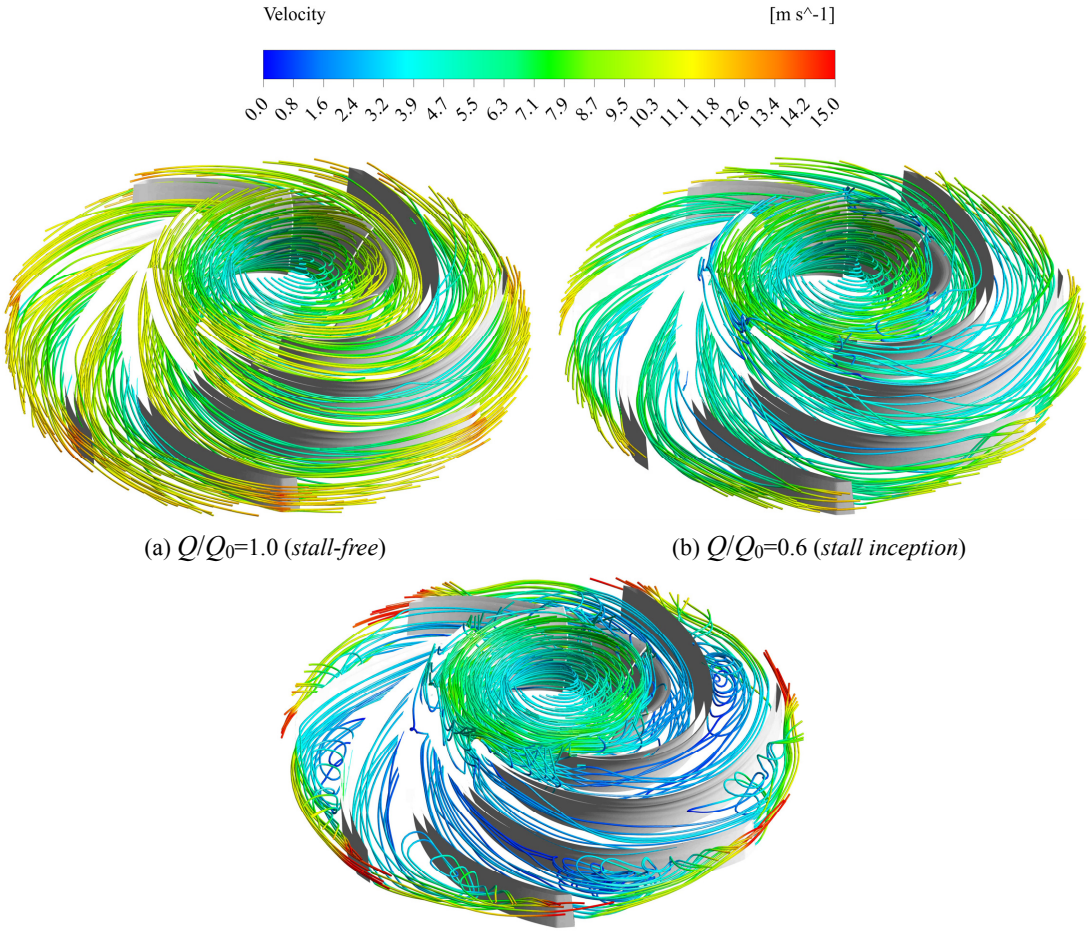

(a) Q/Q_0=1.0 (*stall-free*) (b) Q/Q_0=0.6 (*stall inception*)

(c) Q/Q_0=0.2 (*stall deepening*)

Fig. 13. Time-averaged streamline distributions at different evolution stages

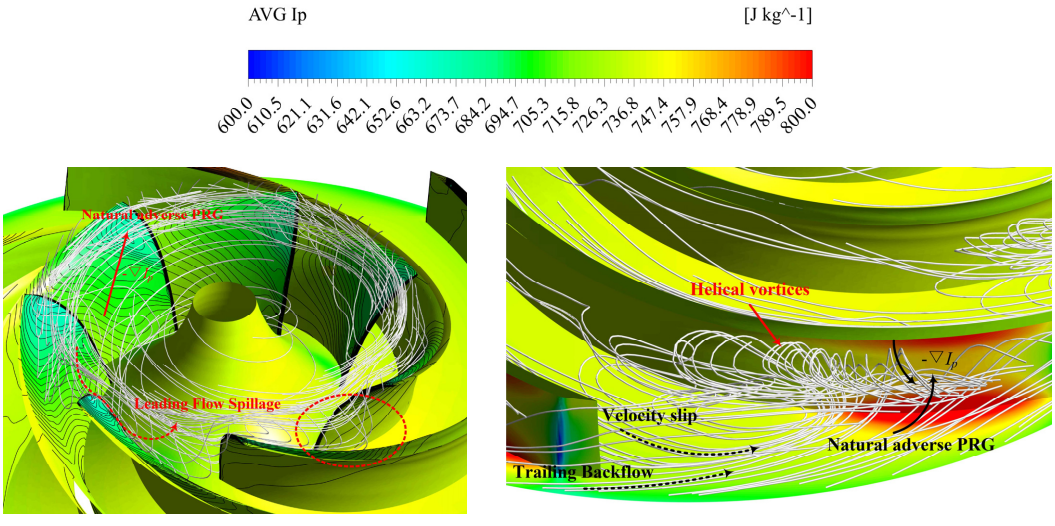

(a) Leading backflow vortices (b) Trailing helical vortices

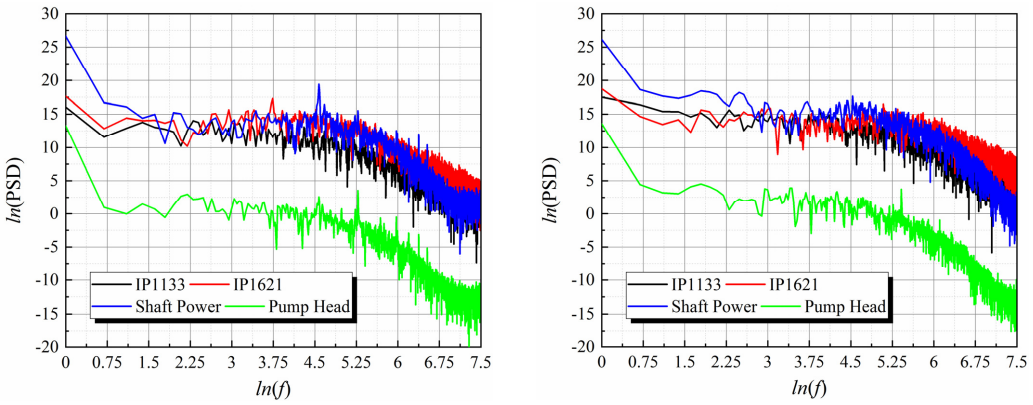

(c) PSD distributions of Q/Q_0=0.6 (d) PSD distributions of Q/Q_0=0.2

Fig. 14. Energetic vortical structures induced by the flow instability

head follow a -21/3 scaling law in a wide range, which implies that the coupling between the vortical signals and the energy signals is very weak at higher frequencies. But at the regions with lower frequencies, a strong coupling between the shaft power P, the pump head H and the rigid vorticity $||\boldsymbol{\omega_R}||_2$ fluctuations is presented, and this effectively proves the interaction between the large-scale vortical motions and the energy conversion instability [69].

5 Summary and conclusions

In this study, the experimental and numerical simulation studies of a centrifugal pump were conducted to clarify the evolution process of energy conversion instability of pump mode in hydro-pneumatic energy storage system, and the conclusions are drawn as follows.

(1) The phenomenon of energy conversion instability is observed in the energy performance test. The slope of the pump head curve $\partial H/\partial Q$ increases in a bumpy way as the pressure ratio rises, and this graded feature first indicates that the instability evolution has a progressive process.

(2) A general diagnostic function *SI* of flow instability in a centrifugal pump is proposed by the authors. According to its diagnosis of inner flow patterns, the energy conversion shows three typical stages. Good inflow stability is presented in the stage of *stall-free* ($SI\approx0.6$) and the corresponding energy conversion is in the stage of *stable work*. The inflow stability is irreversibly damaged in the stage of *stall inception* ($SI\rightarrow1$) and the corresponding energy conversion is in the stage of *stumbled work*. The inflow stability becomes increasingly worse in the stage of *stall deepening* ($SI>1$) and the corresponding energy conversion is in the stage of *shaky work*.

(3) In this evolution process, a quantitative growth model of the energy conversion instability is obtained according to the energy budget analysis. The hydraulic loss ratio increases in a cubic power law as the pressure ratio rises, while the changes in shaft power and pump head fluctuations fit well with the Logistic S-function form of $f(Q)=a+b/(1+(Q/c)^d)$, and the maximum change rate of this S-function occurs at the condition of $SI\approx1$. The flow stability is irreversibly damaged if $SI>1$, and the resultant hydraulic efficiency drop and pressure fluctuation surge can affect the safe and stable operation. Hence, the critical condition for the energy conversion instability is the diagnostic function $SI=1$, and this is recommended for determining the stability limit of the pump mode.

(4) In this evolution process, the attenuation of rotor blade loading gradually spreads from the inlet shroud side to the entire blade and the natural adverse PRG (potential rothalpy gradient) is gradually strengthened. This induces such energetic vortical structures or typical flow events as the

leading backflow vortices, the dynamic stall cells and the trailing helical vortices. A strong coupling at low frequencies between the shaft power, the pump head and the rigid vorticity fluctuations is found according to the PSD (power spectral density) analysis, and this well reveals the interaction between the large-scale vortical motions and the energy conversion instability.

Appendix A: Verification of the numerical simulation scheme

Three meshing schemes, G1, G2 and G3, are proportionally determined and the elements are 2,812,908, 6,216,526 and 13,831,770, respectively. The grid refinement factors, r21 and r32, are approximately 1.3. For the discretization error evaluation, the head of annular cascade regions H_B, the impeller torque M_I, the mean values of rigid vorticity ω_R in the impeller and guide-vane domains and the mean value of total vorticity ω at the impeller exit are taken as the key variables.

The values of the above error evaluation parameters obtained by steady simulations are shown in Table A. 1, including the key evaluation variables φ_1~φ_3, the observed accuracy order A^O, the error ratio $|\varepsilon_{32}/\varepsilon_{21}|$, the extrapolated values φ_{ext}^{21} and φ_{ext}^{32}, the relative errors of extrapolated values e_{ext}^{21} and e_{ext}^{32}, and the grid convergence indices GCI_{fine}^{21} and GCI_{fine}^{32}. Under the $0.2Q_0$ condition, the error ratios are within the range of 0.12~0.67 and it implies that the grid errors will not diverge. The relative errors of the extrapolated values e_{ext}^{32} are within the extent of 0.14%~4.43%, and the values of the grid convergence index GCI_{fine}^{32} are within the extent of 0.18%~5.30%. Therefore, the above meshing schemes can meet the grid convergence requirements. To weigh a balance between the computation cost and the simulation accuracy, the second meshing scheme G2 is finally employed.

Table A. 1 Evaluation results of the discretization error

	H_B / (m)	M_I / (N·m)	$\overline{\omega_{R-imp}}$ / (s^{-1})	$\overline{\omega_{R-van}}$ / (s^{-1})	$\overline{\omega_{imp}}$ / (s^{-1})
φ_1	34.19	151.78	87.50	119.03	3284.46
φ_2	32.06	135.62	85.66	128.48	2270.14
φ_3	31.77	132.53	84.43	133.43	2388.26
A^O	7.60	6.31	1.54	2.46	8.20
$\|\varepsilon_{32}/\varepsilon_{21}\|$	0.14	0.19	0.67	0.52	0.12
φ_{ext}^{21}	34.53	155.60	91.21	108.64	3418.15
e_{ext}^{21}	0.97%	2.46%	4.07%	9.57%	3.91%
GCI_{fine}^{21}	1.31%	3.52%	5.41%	10.11%	7.36%
φ_{ext}^{32}	32.11	136.35	88.14	123.04	2254.57
e_{ext}^{32}	0.14%	0.54%	2.81%	4.43%	0.69%
GCI_{fine}^{32}	0.18%	0.67%	3.62%	5.30%	0.86%

Appendix B: Monitor point scheme in the impeller domain

The monitor point scheme in the impeller domain are determined as follows. As shown in Fig. B. 1(a), the local coordinate system *XYZ* is established and the blade channels are marked as ①~⑦ along the rotating direction. As shown in Fig. B. 1(b), the streamwise coordinates are marked as l=0 and l=1 for the blade inlet and the blade outlet, respectively. Six positions are determined in the streamwise direction and the corresponding coordinates are l=0, l=0.2, l=0.4, l=0.6, l=0.8 and l=1, respectively. The spanwise coordinates are marked as s=0 and s=1 for the hub and the shroud, respectively. Three positions are determined in the spanwise direction and the corresponding coordinates are s=0.1, s=0.5 and s=0.9, respectively. The circumferential coordinates are marked as θ=0 and θ=1 for the blade pressure surface and the blade suction surface. Three positions are

determined in the circumferential direction and the corresponding coordinates are θ=0.2, θ=0.5 and θ=0.8, respectively. Therefore, there are 378 monitor points determined in the whole impeller domain, and each point is named in the form of "IP" + "blade channel position (1~7)" + "streamwise position (1~6)" + "spanwise position (1~3)" + "circumferential position (1~3)".

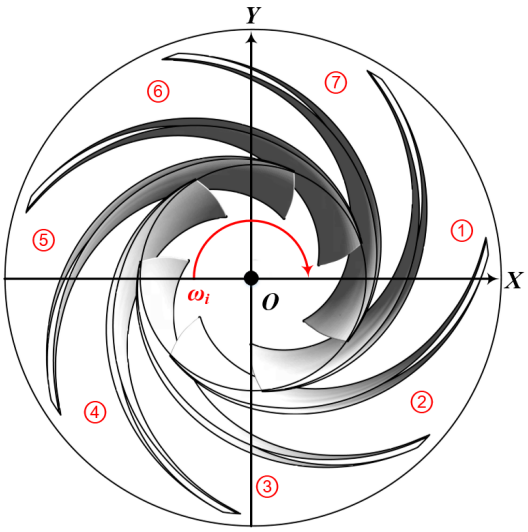

(a) Local coordinate system

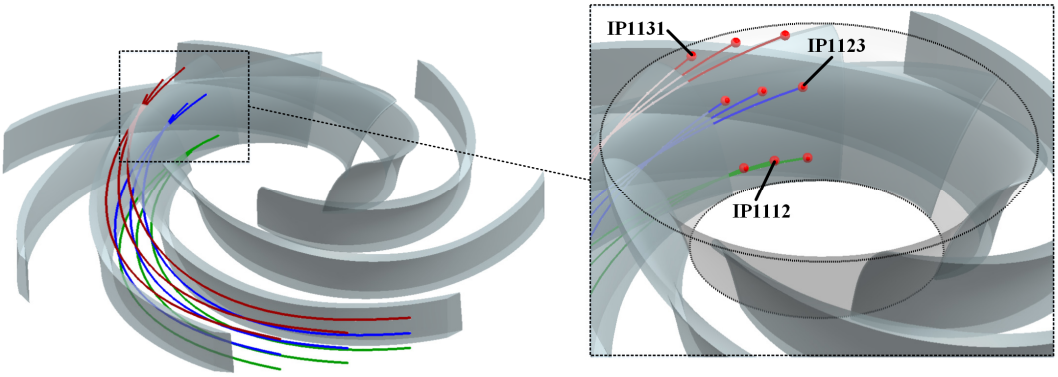

(b) Nomenclature of the monitor points

Fig. B. 1. Monitor point scheme in the impeller domain

Nomenclature

H (H_0)	Pump head (Rated head)
Q (Q_0)	Pump flowrate (Rated flowrate)
P	Shaft power
n	Rotational speed
n_s	Specific speed ($nQ_0^{0.5}/H_0^{0.75}$)
Z	Blade number
D_2	Pump impeller diameter
TSD	Time-scale-driven
δt	Time step
PPV	Peak-to-peak value
$\boldsymbol{V_r}$	Relative velocity vector
I_p	Potential rothalpy

p	Static pressure
$\boldsymbol{\omega_i}$	Rotor angular velocity vector
δp	Rotor blade loading
PRG	Potential rothalpy gradient
$\boldsymbol{F_n}$	Centripetal force
ρ	Density
g	Gravitational acceleration
r^*	Curvature radius
β	Relative flow angle
$\boldsymbol{r}$	Position vector or Real eigenvector
$\boldsymbol{F_C}$	Coriolis force
SI	Diagnostic function
C_m	Meridian velocity
STD	Standard deviation
AVG	Average value
δh	Hydraulic loss
H_i	Impeller head
$\boldsymbol{\omega}$	Total vorticity
$\boldsymbol{\omega_R}$	Rigid vorticity
$\boldsymbol{\omega_S}$	Deformational vorticity
λ_{ci}	Imaginary part of complex conjugate eigenvalues
PSD	Power spectral density
G1, G2, G3	Meshing schemes
r21, r32	Grid refinement factors
H_B	Head of annular cascade regions
M_I	Impeller torque
φ_1, φ_2, φ_3	Key evaluation variables
A^O	Observed accuracy order
$\lvert\varepsilon_{32}/\varepsilon_{21}\rvert$	Error ratio
$\varphi_{\text{ext}}^{21}$, $\varphi_{\text{ext}}^{32}$	Extrapolated values
e_{ext}^{21}, e_{ext}^{32}	Relative errors of extrapolated values
$\text{GCI}_{\text{fine}}^{21}$, $\text{GCI}_{\text{fine}}^{32}$	Grid convergence indices
XYZ	Local coordinate system
l	Streamwise coordinates
s	Spanwise coordinates
θ	Circumferential coordinates

Acknowledgments

The authors would like to acknowledge the financial support given by the National Natural Science Foundation of China (No. 51836010, 51779258, 51839001) and the China Postdoctoral Science Foundation (2021M703516). Besides, we are also grateful to the CAU Fluid Centre for providing the computation hours.

References

[1] Wang H M, Wang G Q, Qi J C, Schandl H, Li Y M, Feng C Y, Yang X C, Wang Y, Wang X Z, Liang S. Scarcity-weighted fossil fuel footprint of China at the provincial level. Applied Energy, 2019; 258: 114081.

[2] Wei Y M, Liao H, Yu B Y, Tang B J. China energy report (2018): green transition in energy intensive sectors. Beijing: Science Press, 2018.

[3] Kocaman A S, Modi V. Value of pumped hydro storage in a hybrid energy generation and allocation system. Applied Energy, 2017; 205: 1202-1215.

[4] Silva G O, Hendrick P. Pumped hydro energy storage in buildings. Applied Energy, 2016; 179: 1242-1250.

[5] Yan J Y. Handbook of clean energy systems. John Wiley & Sons, Ltd., 2015.

[6] Rahman M M, Oni A O, Gemechu E, Kumar A. Assessment of energy storage technologies: A review. Energy Conversion and Management, 2020; 223: 113295.

[7] Shabani M, Dahlquist E, Wallin F, Yan J Y. Techno-economic comparison of optimal design of renewable-battery storage and renewable micro pumped hydro storage power supply systems: A case study in Sweden. Applied Energy, 2020; 279: 115830.

[8] Ferreira H L, Garde R, Fulli G, Kling W, Lopes J P. Characterisation of electrical energy storage technologies. Energy, 2013; 53: 288-298.

[9] Chen H S, Liu C, Xu Y J, Yue F, Liu W, Yu Z H. The strategic position and role of energy storage under the goal of carbon peak and carbon neutrality. Energy Storage Science and Technology, 2021; 10(5): 1477-1485.

[10] Zhang S F, Andrews-Speed P, Perera P. The evolving policy regime for pumped storage hydroelectricity in China: A key support for low-carbon energy. Applied Energy, 2015; 150: 15-24.

[11] Rehman S, Al-Hadhrami L M, Alam M M. Pumped hydro energy storage system: A technological review. Renewable and Sustainable Energy Reviews, 2015; 44: 586-598.

[12] Venkataramani G, Ramalingam V, Viswanathan K. Harnessing free energy from nature for efficient operation of compressed air energy storage system and unlocking the potential of renewable power generation. Scientific Reports, 2018; 8: 9981.

[13] Mouli-Castillo, Wilkinson M, Mignard D, McDermott C, Haszeldine R S, Shipton Z K. Inter-seasonal compressed-air energy storage using saline aquifers. Nature Energy, 2019; 4: 131-139.

[14] Olabi A G, Wilberforce T, Ramadan M, Abdelkareem M A, Alami A H. Compressed air energy storage systems: Components and operating parameters-A review. Journal of Energy Storage, 2021; 34: 102000.

[15] Wang H, Tong Z R, Dong X, Xiong W, Ting D S K, Carriveau R, Wang Z W. Design and energy saving analysis of a novel isobaric compressed air storage device in pneumatic systems. Journal of Energy Storage, 2021; 38: 102614.

[16] Saad Y, Younes R, Abboudi S, Ilinca A. Hydro-pneumatic storage for wind-diesel electricity generation in remote sites. Applied Energy, 2018; 231: 1159-1178.

[17] Javed M S, Zhong D, Ma T, Song A, Ahmed S. Hybrid pumped hydro and battery storage for renewable energy based power supply system. Applied Energy, 2020; 257: 114026.

[18] Tobajas J, Garcia-Torres F, Roncero-Sánchez P, Vázquez J, Bellatreche L, Nieto E. Resilience-oriented schedule of microgrids with hybrid energy storage system using model predictive control. Applied Energy, 2022; 306: 118092.

[19] Kim Y M, Favrat D. Energy and exergy analysis of a micro-compressed air energy storage and air cycle heating and cooling system. Energy, 2010; 35: 213-220.

[20] Kim Y M, Shin D G, Favrat D. Operating characteristics of constant-pressure compressed air energy storage (CAES) system combined with pumped hydro storage based on energy and exergy analysis. Energy, 2011; 36: 6220-6233.

[21] Petric J. Modeling of hydro-pneumatic energy storage system. 8th EUROSIM Congress on Modelling and

Simulation, 2013.

[22] Wang H R, Wang L Q, Wang X B, Yao E. A novel pumped hydro combined with compressed air energy storage system. Energies, 2013; 6: 1554-1567.

[23] Yao E, Wang H R, Liu L, Xi G. A novel constant-pressure pumped hydro combined with compressed air energy storage system. Energies, 2015; 8: 154-171.

[24] Chen H, Wang H R, Li R X, Zhang Y, He X. Thermo-dynamic and economic analysis of s a novel near-isothermal pumped hydro compressed air energy storage system. Journal of Energy Storage, 2020; 30: 101487.

[25] Yi T, Ma F, Jin C, Huang Y J. A novel coupled hydro-pneumatic energy storage system for hybrid mining trucks. Energy, 2018; 143: 704-718.

[26] Buhagiar D, Sant T. Modelling of a novel hydro-pneumatic accumulator for large-scale offshore energy storage applications. Journal of Energy Storage, 2017; 14: 283-294.

[27] Sant T, Buhagiar D, Farrugia R N. Evaluating a new concept to integrate compressed air energy storage in spartype floating offshore wind turbine structures. Ocean Engineering, 2018; 166: 232-241.

[28] Buhagiar D, Sant T, Farrugia R N. Hydro-pneumatic energy storage. Reference Module in Earth Systems and Environmental Sciences, Elsevier, 2021.

[29] Bi X Y, Liu P, Li Z. Thermo-dynamic analysis and simulation of a combined air and hydro energy storage (CAHES) system. Energy, 2016; 116: 1385-1396.

[30] Mozayeni H, Wang X L, Negnevitsky M. Thermodynamic and exergy analysis of a combined pumped hydro and compressed air energy storage system. Sustainable Cities and Society, 2019; 48: 101527.

[31] Marefati M, Mehrpooya M, Pourfayaz F. Performance analysis of an integrated pumped-hydro and compressed-air energy storage system and solar organic Rankine cycle. Journal of Energy Storage, 2021; 44: 103488.

[32] Yin J L, Wang D Z, Kim Y T, Lee Y H. A hybrid energy storage system using pump compressed air and micro-hydro turbine. Renewable Energy, 2014; 65: 117-122.

[33] Odukomaiya A, Abu-Heiba A, Graham S, Momen A M. Experimental and analytical evaluation of a hydro-pneumatic compressedair Ground-Level Integrated Diverse Energy Storage (GLIDES) system. Applied Energy, 2018; 221: 75-85.

[34] Sampedro E O. Étude d'un système hydropneumatique de stockage d'énergie utilisant une pompe/turbine rotodynamique. École Nationale Supérieure d'Arts et Métiers, 2013.

[35] Sampedro E O, Dazin A, Colas F, Roussette O, Coutier-Delgosha O, Caignaert G. Multistage radial flow pump-turbine for compressed air energy storage: Experimental analysis and modeling. Applied Energy, 2021; 289: 116705.

[36] Kalaiselvan A S V, Subramaniam U, Shanmugam P, Hanigovszki N. A comprehensive review on energy efficiency enhancement initiatives in centrifugal pumping system. Applied Energy, 2016; 181: 495-513.

[37] Gülich J F. Centrifugal pumps. Springer Nature Switzerland, 2020.

[38] Zuo Z G, Liu S H. Flow-induced instabilities in pump-turbines in China. Engineering, 2017; 3: 504-511.

[39] Li D Y, Wang H J, Qin Y L, Han L, Wei X Z, Qin D Q. Entropy production analysis of hysteresis characteristic of a pump-turbine model. Energy Conversion and Management, 2017; 149: 175-191.

[40] Li D Y, Chang H, Zuo Z G, Wang H J, Li Z G, Wei X Z. Experimental investigation of hysteresis on pump performance characteristics of a model pump-turbine with different guide vane openings. Renewable Energy, 2020; 149: 652-663.

[41] Li D Y, Zuo Z G, Wang H J, Liu S H, Wei X Z, Qin D Q. Review of positive slopes on pump performance characteristics of pump-turbines. Renewable and Sustainable Energy Reviews, 2019; 112: 901-916.

[42] Ran H J, Luo X W. Experimental study of instability characteristics in pump turbines. Journal of Hydraulic

Research, 2018; 56(6): 871-876.

[43] Yang D D, Luo X W, Liu D M, Huang R F, Zhu Z C. Unstable flow characteristics in a pump-turbine simulated by a modified Partially-Averaged Navier-Stokes method. SCIENCE CHINA-Technological Sciences, 2019; 62(3): 406-416.

[44] Ran H J, Liu Y, Luo X W, Shi T J, Xu Y L, Chen Y L, Wang D Z. Experimental comparison of two different positive slopes in one single pump turbine. Renewable Energy, 2020; 154: 1218-1228.

[45] Liu Y, Wang D Z, Ran H J. Computational research on the formation mechanism of double humps in pump-turbines. Engineering Applications of Computational Fluid Mechanics, 2021; 15(1): 1542-1562.

[46] Li X J, Zhu Z C, Li Y, Chen X P. Experimental and numerical investigations of head-flow curve instability of a single-stage centrifugal pump with volute casing. Proceedings of the Institution of Mechanical Engineers Part A-Journal of Power and Energy, 2016; 230(A7): 633-647.

[47] Feng J J, Ge Z G, Yang H H, Zhu G J, Li C H, Luo X Q. Rotating stall characteristics in the vaned diffuser of a centrifugal pump. Ocean Engineering, 2021; 229: 108955.

[48] Wang W J, Pavesi G, Pei J, Yuan S Q. Transient simulation on closure of wicket gates in a high-head Francis-type reversible turbine operating in pump mode. Renewable Energy, 2020; 145: 1817-1830.

[49] Dazin A, Caignaert G, Bois G. Transient behavior of turbomachineries: Applications to radial flow pump startups. Journal of Fluids Engineering, 2007; 129(11): 1436-1444.

[50] Li Z F, Wu D Z, Wang L Q, Huang B. Numerical simulation of the transient flow in a centrifugal pump during starting period. Journal of Fluids Engineering, 2010; 132(8): 081102.

[51] Liu J, Li Z, Wang L, Jiao L. Numerical simulation of the transient flow in a radial flow pump during stopping period. Journal of Fluids Engineering, 2011; 133(11): 111101.

[52] Hasmatuchi V. Hydrodynamics of a pump-turbine operating at off-design conditions in generating mode. École Polytechnique Fédérale De Lausanne, 2012.

[53] Pacot O, Kato C, Guo Y, Yamade Y, Avellan F. Large eddy simulation of the rotating stall in a pump-turbine operated in pumping mode at a part-load condition. Journal of Fluids Engineering, 2016; 138(11): 111102.

[54] Liu D M, Xu W L, Zhao Y Z. Experimental study of the flow field of a high head model pump turbine based on PIV technique. Journal of Hydrodynamics, 2021; 33(5): 1045-1055.

[55] Guo H, Xu Y J, Zhang Y, Liang Q, Tang H T, Zhang X J, Zuo Z T, Chen H S. Off-design performance and an optimal operation strategy for the multistage compression process in adiabatic compressed air energy storage systems. Applied Thermal Engineering, 2019; 149: 262-274.

[56] Guo W B, Zuo Z T, Sun J T, Hou H C, Liang Q, Chen H S. Experimental investigation on off-design performance and adjustment strategies of the centrifugal compressor in compressed air energy storage system. Journal of Energy Storage, 2021; 38: 102515.

[57] Krenn J, Keck H, Sallaberger M. Small and mid-size pump-turbines with variable speed. Energy and Power Engineering, 2013; 5(2): 48-54.

[58] Lu L, Meng X C. Pump model test report of Niulan River-Tien Lake Water Supplement Project. China Institute of Water Resources and Hydropower Research, 2010.

[59] Wang C Y, Wang F J, An D S, Yao Z F, Xiao R F, Lu L, He C L, Zou Z C. A general alternate loading technique and its applications in the inverse designs of centrifugal and mixed-flow pump impellers. Science China-Technological Sciences, 2021; 64(4): 898-918.

[60] Wang C Y, Wang F J, Li C F, Ye C L, Yan T T, Zou Z C. A modified STRUCT model for efficient engineering computations of turbulent flows in hydro-energy machinery. International Journal of Heat and Fluid Flow, 2020; 85: 108628.

[61] Wang C Y, Wang F J, Ye C L, Wang B H, Zou Z C. Application of the MST turbulence model to predict the tip

leakage vortex flows. Engineering Computations, 2021; 38(1): 344-353.

[62] Wang C Y. Investigation on stall flow analysis methods and stall characteristics of centrifugal pump. China Agricultural University, 2021.

[63] Day I J. Stall, surge and 75 years of research. Journal of Turbomachinery, 2016; 138(1): 011001.

[64] Tao R, Wang Z W. Comparative numerical studies for the flow energy dissipation features in a pump-turbine in pump mode and turbine mode. Journal of Energy Storage, 2021; 41: 102835.

[65] Liu C Q, Gao Y S, Tian S L, Dong X R. Rortex-A new vortex vector definition and vorticity tensor and vector decompositions. Physics of Fluids, 2018; 30: 035103.

[66] Wang Y Q, Gao Y S, Liu J M, Liu C Q. Explicit formula for the Liutex vector and physical meaning of vorticity based on the Liutex-shear decomposition. Journal of Hydrodynamics, 2019; 31(3): 464-474.

[67] Wang C Y, Zeng Y S, Yao Z F, Wang F J. Rigid vorticity transport equation and its application to vortical structure evolution analysis in hydro-energy machinery. Engineering Applications of Computational Fluid Mechanics, 2021; 15(1): 1016-1033.

[68] Tan C S, Day I, Morris S, Wadia A. Spike-type compressor stall inception, detection, and control. Annual Review of Fluid Mechanics, 2010; 42: 275-300.

[69] Ahmadi M H B, Yang Z Y. On wind turbine power fluctuations induced by large-scale motions. Applied Energy, 2021; 293: 116945.